Supporting Information: **Thermal conductivity of Bi₂Te₃ nanowires: How size affects phonon scattering**

Miguel Muñoz Rojo[1†], B. Abad[1†], C. V. Manzano[1], P. Torres[2], X. Cartoixá[3], X. Alvarez[2], and M. Martín Gonzalez[1]*

[1] IMM-Instituto de Microelectrónica de Madrid (CNM-CSIC), Isaac Newton 8, PTM, Tres Cantos, Madrid, 28760, Spain.

[2] Departament de Física, Universitat Autònoma de Barcelona, Bellaterra, Catalonia, 08193, Spain.

[3] Departament d'Enginyeria Electrònca, Universitat Autònoma de Barcelona, Bellaterra, Catalonia, 08193, Spain.

†Both authors contributed equally to work.

Compositional characterization: Energy dispersive X-ray (EDX)

Table S1. The atomic % values of Bismuth and tellurium according to the EDX analysis of bismuth telluride nanowires templates of 300 nm, 52 nm, 45 nm and 25 nm.

Diameter of Bi₂Te₃ nanowires	Atomic % Bismuth	Atomic % Tellurium	Formula
300 nm	38 ± 2	62 ± 2	
52 nm	40 ± 2	60 ± 2	Bi₂Te₃
45 nm	39 ± 2	61 ± 2	
25 nm	41± 2	59± 2	

Structural characterization: X-Ray diffraction patterns

The crystallinity of the four samples was investigated the X-ray diffractrograms which are showed in Figure S1. The strongest diffraction peak is (1 1 0), which is located at 41.148 º. The (3 0 0) peak is also found at 74.955 º. The samples also show the (2 2 0) at 89.278 º showing that the wires show a high preferential orientation along [1 1 0]. Therefore, the *c-axis* is perpendicular to the nanowire long

direction in all the cases. The grain size was estimated to be ~10 μm. Since boundary scattering limit the phonons with mean free path larger than the wire diameter (D<<10μm), the estimated grain size does not affect the thermal conductivity of the present samples.
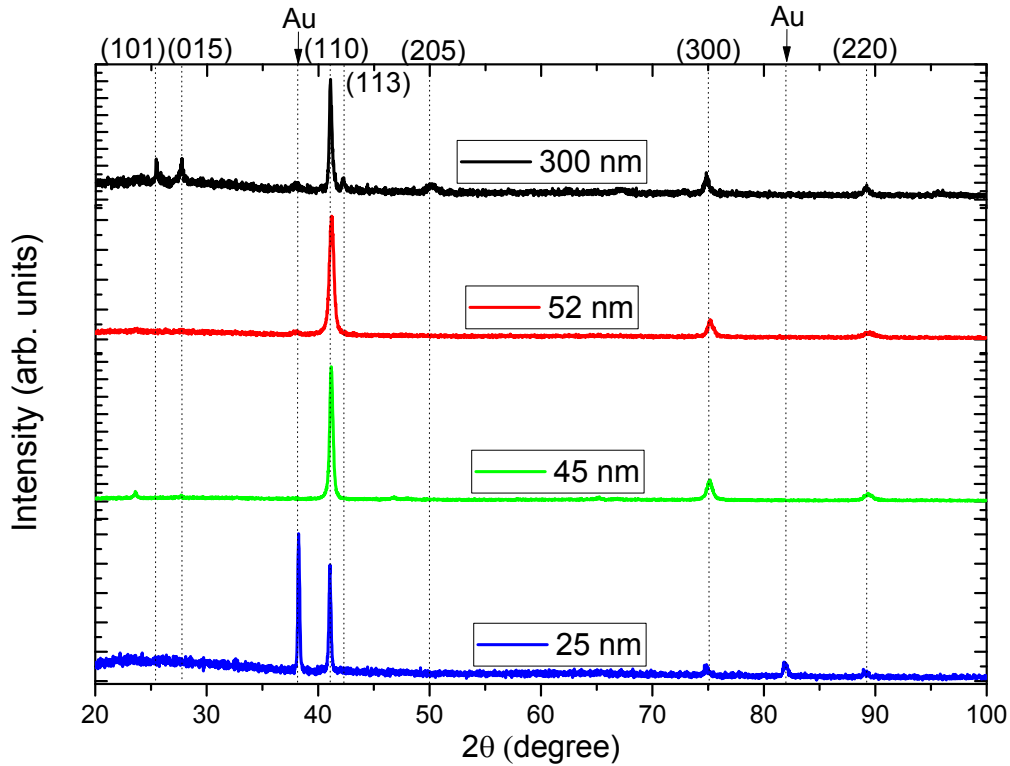

Figure S1. X-ray diffractograms of the bismuth telluride nanowire templates of 300nm, 52nm, 45nm and 25 nm. The *c-axis* of the Bi_2Te_3 structure is perpendicular to the nanowire axis.

Mechanical polishing

Bi_2Te_3 nanowires embedded in alumina templates were polished by mechanical polishing in order to remove any overgrown structure and achieve a flat surface with the tips of the nanowires at the alumina surface level. The polish process was carried out by gluing the sample to the center of a polishing holder while a constant pressure from its own weight was applied. A continuous spinning at low revolution per minute (rpm) was employed to avoid cracks or damage

in the composite. A polishing cloth along with alumina powders of different particle size, 1 μm, 0.5 μm and 0.03 μm, were used. The size of the alumina particles were gradually reduced from 1μm to 0.03 μm in such a way that a final roughness of less than 20 nm was achieved.

Photoacoustic technique

The thermal conductivity of the NWs embedded into the matrix could be measured by the PA technique. The thermal conductivity measurements of the nanowire embedded in the AAO matrix are performed by evaporating 80 nm titanium layer onto the surface where the gold was previously deposited in order to absorb the laser beam. The gold layer was studied to not influence the measurement as it can be considered as a part of the thermal contact resistance between the titanium and the alumina membrane. The experimental data obtained is used to obtain the composite thermal conductivity by means of the theoretical model proposed by Hu et al [1].
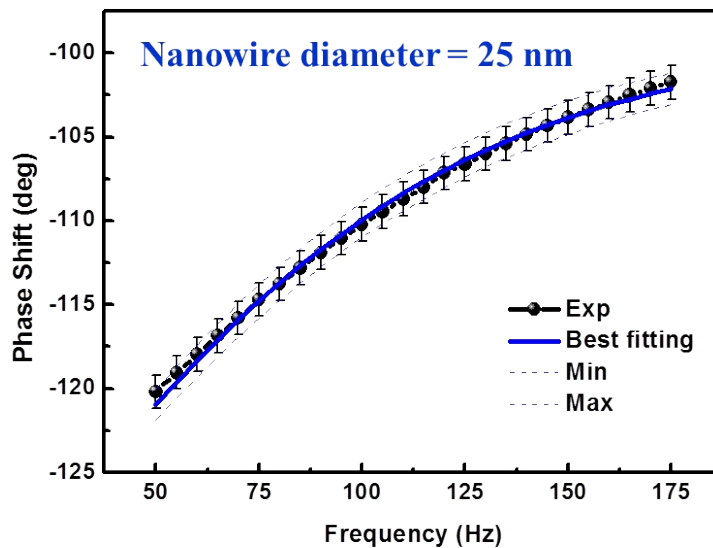
Figure S2. Data fitting of the experimental data obtained by the PA technique for the 30 nm nanowires embedded into the alumina membrane.

As an example, Figure S2 shows the fitted experimental data for the 25.nm sample. The uncertainty analysis of this type of structures can be found elsewhere[2].

Scanning Thermal Microscopy (SThM)

The thermal conductivity measurements of some of the Bi_2Te_3 NWs were carried out using a scanning thermal microscope (SThM) working in 3ω mode.

The SThM has been successfully used to measure the thermal conductivity of films, nanowires [3] [4] [5] [6] [7] or nanomeshes[8]. An atomic force microscope (AFM) from Nanotec® Company and a Wollaston thermoresistive probes from Bruker® were used to carry out the thermal scans on the samples. We summarize the working procedure, which is explained in detail in reference [3] .

In order to measure the thermal conductivity of the nanowires arrays with the SThM, a Wollaston thermo-resistive probe was brought into contact with the sample and measured the 3ω-voltage in several locations. Then, from studying several location of the sample, similar to the statistical analysis presented in reference [3], the equivalent thermal resistance of the sample can be determined. This equivalent thermal resistance can be expressed in two terms[6] [7],

$$R_{eq} = R_C + R_{comp}$$

where R_{comp}, is the thermal resistance of the composite, i.e. the Bi_2Te_3 nanowires and the alumina at which they are embedded, while, R_c, is the contact resistance between the probe and the sample surface. As the contact resistance was determined from the calibration of the probe, the composite thermal resistance can be calculated from the previous equation. Then, due to the long length of the NWs (around 30 μm) and because of the thermal exchange radius of the probe, b, is also known from the calibration process, the semi-infinite medium theory can be used to obtain the thermal conductivity of the composite, k_{comp}, [6] [7]

$$R_{comp} = \frac{1}{4k_{comp}b}$$

Finally, in order to determine the thermal conductivity of the intrinsic nanowire, the effective medium theory can be used.

The calibration [3] of the probe is essential to determine quantitatively the thermal conductivity of the sample. The thermal exchange radius, b, and the contact resistance, Rc, between the probe and the sample are obtained from this process. As explained in ref. [3], when the thermal conductivity of the sample measure remains between 0.1 W/K·m and ~3 W/K·m, the thermal exchange radius and contact resistance remains the same. A set of calibrating samples with well-defined thermal conductivity in this range were measured, as explained in ref [3]. The calibration samples were made of polyaniline (PANI) with 5% and 7% graphene platelets and a borosilicate glass with thermal conductivities of k=0.49 W/K·m, k=0.65 W/K·m and k=1.1 W/K·m, respectively. Since the thermal conductivity of these sample is known, the contact resistance *vs* the thermal exchange radius resulting from iteration methods can be plotted, as explained in ref [3]. Figure S3 shows the crossing between those curves, resulting in a value of

b=(2.27±0.09) µm and Rc= 29365±6925 (K/W). The probe convection coefficient was determined to be, h=3324 W/K·m². Two more samples with well know thermal conductivities (tellurium, k=0.75W/Km and silicon germanium k=1.2W/Km) were also measured as a cross check, resulting in good agreement. This probe has been also used to measure SiGe nanomeshes[8].
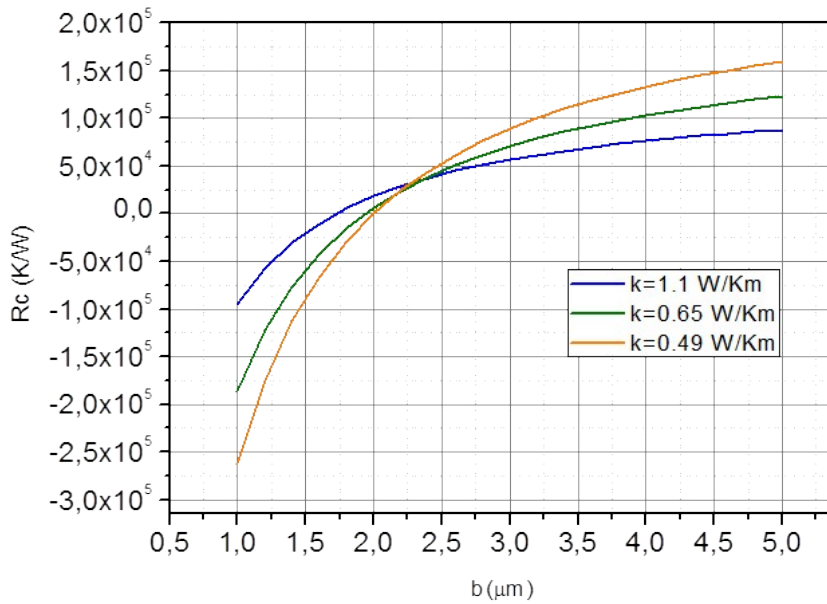

Figure S3. Thermal exchange radius vs contact resistance graph obtained during the calibration process for the Wollaston probe used.

Data analysis

As explained along the manuscript, the SThM was mainly used to support the trend observed by the PA technique. In Table S2, the measurements obtained from the SThM and the PA technique are shown. The good agreement observed for both technique for the 45nm diameter sample,

within the uncertainty, suggests that the measurements obtained from PA are reliable and that the trend is correct. Although other Bi_2Te_3 nanowires were measured with the SThM, their composition varied slightly respect to the proper one and were not considered in this analysis.

Table S2. Summary of the thermal results obtained for different [110] stoichiometric Bi_2Te_3 diameter nanowire arrays measured by different techniques. All of the measurements are done in the out-of-plane direction. Sample 45 nm was measured by both techniques for comparison.

NW Diameter average (nm)	Crystalline Orientation	Thermal conductivity composite (W/K·m)	Technique	Porosity (%)	Calculated Filling factor ±5 % (%)	Thermal conductivity [110] Bi_2Te_3 NWs and film (W/K·m)
300±75	[110]	1.52±0.20	SThM	49±5	97	1.78±0.46
52±5	[110]	1.06±0.09	PA	35±2	79	0.72±0.37
45± 4	[110]	1.09±0.10	PA	28±2	85	0.58±0.47
		1.07±0.10	SThM			0.50±0.47
25±4	[110]	0.83±0.05	PA	34±4	70	0.52±0.35

The thermal conductivity composite uncertainty was obtained differently for each technique. In the case of the PA technique, the procedure to calculate the composite thermal conductivity could be found elsewhere [2]. For the SThM technique, the procedure to determine the thermal conductivity of the measured sample can be found in [3].

Once the thermal conductivity composite was obtained, the nanowire thermal conductivity was calculated by means of the effective medium theory described by Equation 3. In order to calculate the associated uncertainty, we carried out the propagation of errors given by:

$$\Delta z = \sqrt{\sum_{i=1}^{N}\left(\frac{\partial z}{\partial Y_i}\Delta Y_i\right)^2}$$

Where z is the magnitude whose uncertainty is calculated and Y_i is each of the magnitudes involved in the calculation of the nanowire thermal conducivity, i.e., porosity, composite thermal conductivity, alumina thermal conductivity and filling factor. Table S2 shows that the uncertainties associated to the PA and SThM measurements are ~10% maximum. However, the final value of the thermal conductivity of the nanowires or lattice thermal conductivity is much larger. This is consequence of taking into account all the possible error sources that contribute to the uncertainty, i.e. the thermal conductivity of the alumina template, porosity, electrical conductivity, etc. Despite having a large error, the clear trend observed for the thermal conductivity, the fact that the ends of the experimental error bars follow a similar trend and the fact that an independent technique (SThM) obtains similar results (see Table S2) demonstrate that the data measured is accurate.

Kinetic Collective Model (KCM)

The Kinetic-Collective model is in the framework of the Boltzmann transport equation as a generalization of the Guyer-Krumhansl model including the effects of the dispersion [9] [10]. This model incorporates the role of normal scattering in the current footing. Although normal scattering is a non-resistive process, its presence has a deep effect on thermal conductivity due to the distribution of energy that generates. When normal scattering is not important, thermal conductivity can be calculated with the usual kinetic expression, that is

$$\kappa_k = \int c_{v\omega} v_\omega^2 \tau_\omega d\omega$$

where c_v is the mode specific heat, υ the velocity and τ the total relaxation time. The total relaxation time is obtained by combining using the Mathiessen rule only the resistive scattering times, that is, umklapp, impurity and boundary.

$$\tau_\omega^{-1} = \tau_{B\omega}^{-1} + \tau_{I\omega}^{-1} + \tau_{U\omega}^{-1}$$

All the three scattering times are calculated and does not contain any fitting parameter. For the boundary term we use

$$\tau_{B\omega}^{-1} = \frac{D}{v_\omega}$$

where L is the diameter of the wire, and for the impurity

$$\tau_I^{-1} = D \cdot \omega^4$$

with $D = \gamma \cdot V/(4 \cdot \pi \cdot v^3)$ where γ is the mass variance, V the atomic volume and v the phonon velocity.

In this case, each mode contributes independently to the rest of the distribution. That it means that the presence of a large scattering in one mode does not affect the propagation of the rest of the modes.

When normal scattering becomes important, this behavior is significantly changed. Despite its non-resistive nature, normal scattering redistributes energy over all the modes and homogenize the distribution. If a mode is highly affected by some scattering mechanism, normal scattering will refill that mode with energy coming from the rest of the distribution. That means that the scattering suffered by this mode will be noticed by the rest of the modes due to the connection provided by normal scattering. When normal scatteting is dominant

$$k_c = \int c_{v\omega} v_\omega^2 \tau_c d\omega$$

where τ_c, the collective relaxation time, is the averaged inverse relaxation time over all the modes of the distribution

$$\tau_c = \frac{\int c_{v\omega} v_\omega^2 d\omega}{\int \frac{c_{v\omega} v_\omega^2}{\tau_\omega} d\omega}$$

The physical interpretation of this change in the relaxation time depending on the presence of normal scattering can be understood by a simple equivalence. Kinetic regime is like combining electrical resistors in paral·lel and collective regim like combine them in series. In the kinetic regime, each model notice a different resistance, while in the collective regime it notice all the resistances. By this equivalence it can be understood the average of the inverse of the relaxation times.

This model has been used to obtain the thermal conductivity of bulk and nanostructures, such as nanowires, and understand the reduction due to the dimensionality as a change from collective to kinetic regime. As a consequence, two different thermal transport regimes could be established, i.e. the kinetic and the collective, which depend on what scattering mechanism (resistive or normal) is dominating the transport. While in the kinetic regime each phonon contributes independently to the heat flux, in the collective regime the momentum is conserved and shared among the phononic modes (the phonons behave as a whole). The Kinetic-Collective model can be applied to any range of temperature and provide a new insight into the underlying physics of thermal transport, introducing thermodynamic perspective at mesoscopic level that allows the interpretation of the differences in phonon behavior in terms of the average of the phonon-phonon processes.

First principles simulation details

Bi_2Te_3 thermal conductivity from *first principles* have been obtained under the Density

Functional Theory (DFT) using the VASP package [11] [12] [13] [14] in the Local Density Approximation (LDA). LDA pseudopotentials in the parametrization of Perdew and Zunger are used [15]. Plane waves are cut off at 300 eV. For the simulations a 3x3x1 supercell with 135 atoms obtained from the 15-atoms hexagonal cell is used. Dispersion relations (DR), Density Of States (DOS) and harmonic and anharmonic Interatomic Force Constants (IFC) have been calculated in a 3x3x2 k-point grid.

To obtain Normal and Umklapp Bi_2Te_3 three phonon scattering relaxation times we used Phono3py [16] with the IFC obtained from VASP. The manual implementation of the splitting of Normal and Umklapp processes is done according to the crystalline momentum conservation, where for Normal processes $k_1=k_2+k_3$ (or $k_1+k_2=k_3$) and for Umklapp processes $k_1=k_2+k_3+G$ (or $k_1+k_2=k_3+G$), being G a reciprocal grid vector. The latter have been calculated in a 24x24x8 k-point grid. Figure S4 shows the obtained Normal and Umklapp relaxation times.
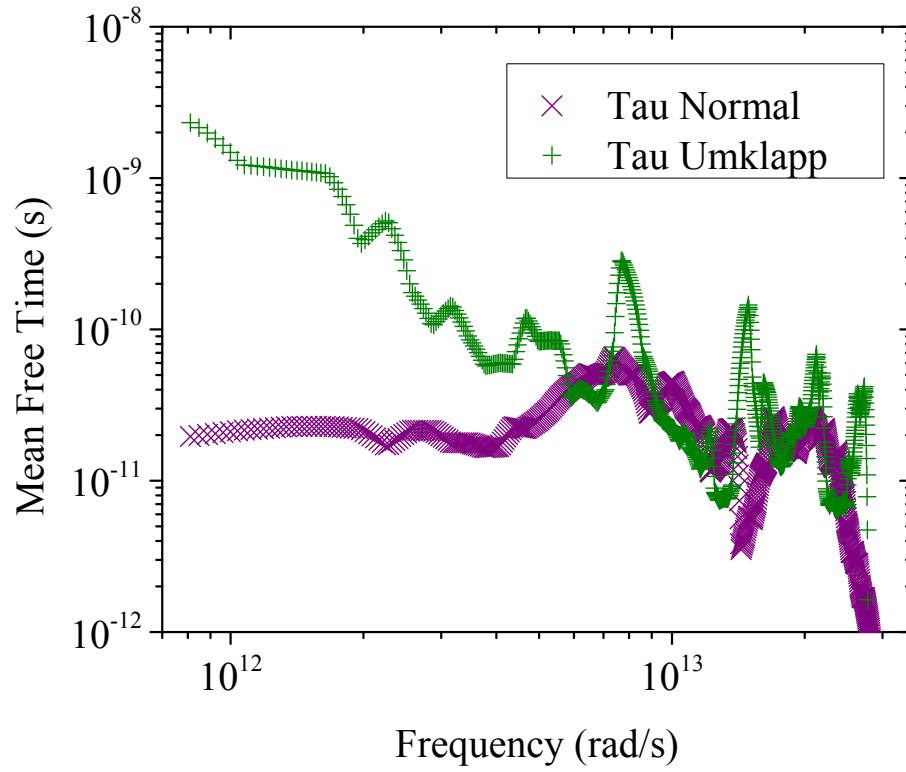
Figure S4. Normal and Umklapp relaxation times in terms of frequency at 300K.

References

1 H. Hu, X. Wang and X. Xu, *J. Appl. Phys.*, 1999, **86**, 3953.

2 B. Abad, J. Maiz and M. Martin-Gonzalez, *J. Phys. Chem. C*, 2016, **120**, 5361–5370.

3 A. A. Wilson, M. Muñoz Rojo, B. Abad, J. A. Perez, J. Maiz, J. Schomacker, M. Martín-Gonzalez, D.-A. Borca-Tasciuc and T. Borca-Tasciuc, *Nanoscale*, 2015, **7**, 15404–15412.

4 J. Maiz, M. Muñoz Rojo, B. Abad, A. A. Wilson, A. Nogales, D.-A. Borca-Tasciuc, T. Borca-Tasciuc and M. Martín-González, *RSC Adv.*, 2015, **5**, 66687–66694.

5 M. Muñoz Rojo, O. Caballero Calero, a F. Lopeandia, J. Rodriguez-Viejo and M. Martín-Gonzalez, *Nanoscale*, 2013, **5**, 11526–44.

6 M. Muñoz Rojo, J. Martín, S. Grauby, T. Borca-Tasciuc, S. Dilhaire and M. Martin-Gonzalez, *Nanoscale*, 2014, **6**, 7858–7865.

7 M. Muñoz Rojo, S. Grauby, J.-M. Rampnoux, O. Caballero-Calero, M. Martin-Gonzalez and S. Dilhaire, *J. Appl. Phys.*, 2013, **113**, 54308.

8 J. A. Pérez-Taborda, M. Muñoz-Rojo, J. Maiz, N. Neophytou and M. Martín-González, *Sci. Rep.*, 2016, **6**, 32778

9 C. De Tomas, A. Cantarero, A. F. Lopeandia and F. X. Alvarez, *J. Appl. Phys.*, 2014, **115**, 0–11.

10 C. de Tomas, A. Cantarero, a F. Lopeandia and F. X. Alvarez, *Proc. R. Soc. A Math. Phys. Eng. Sci.*, 2014, **470**, 20140371–20140371.

11 G. Kresse and J. Hafner, *Phys. Rev. B*, 1993, **47**, 558–561.

12 G. Kresse and J. Hafner, *Phys. Rev. B*, 1994, **49**, 14251–14269.

13 G. Kresse and J. Furthmüller, *Comput. Mater. Sci.*, 1996, **6**, 15–50.

14 G. Kresse and J. Furthmüller, *Phys. Rev. B*, 1996, **54**, 11169–11186.

15 J. P. Perdew and A. Zunger, *Phys. Rev. B*, 1981, **23**, 5048–5079.

16 A. Togo, L. Chaput and I. Tanaka, *Phys. Rev. B - Condens. Matter Mater. Phys.*, 2015, **91**, 094306.